INDIAN JOURNAL OF PHYSICS
Accepted June 16th 2017
ISSN: 0973-1458 (print version)
ISSN: 0974-9845 (electronic version)
Impact Factor = 1.166
Publisher= Springer

FINITE ELEMENT COMPUTATION OF MULTI-PHYSICAL MICROPOLAR TRANSPORT PHENOMENA FROM AN INCLINED MOVING PLATE IN POROUS MEDIA

MD. Shamshuddin[1*], O. Anwar Bég[2], M. Sunder Ram[3] and A. Kadir[4]

[1*]*Department of Mathematics, Vaagdevi College of Engineering (Autonomous), Warangal, Telangana,* ***India****.*
[2]*Fluid Mechanics, Aeronautical and Mechanical Engineering, School of Computing, Science and Engineering, Newton Building, The Crescent, Salford, M54WT, England,* ***UK.***
[3]*Department of Mathematics, Chaitanya Degree College (Autonomous), Warangal, Telangana,* ***India****.*
[4]*Corrosion and Materials, Petroleum and Gas Engineering, School of Computing, Science and Engineering, Newton Building, The Crescent, Salford, M54WT, England,* ***UK.***

**Corresponding author:* shammaths@gmail.com

Abstract: Non-Newtonian flows arise in numerous industrial transport processes including materials fabrication systems. Micropolar theory offers an excellent mechanism for exploring the fluid dynamics of new non-Newtonian materials which possess internal microstructure. Magnetic fields may also be used for controlling electrically-conducting polymeric flows. To explore numerical simulation of transport in rheological materials processing, in the current paper, a finite element computational solution is presented for magnetohydrodynamic (MHD), incompressible, dissipative, radiative and chemically-reacting micropolar fluid flow, heat and mass transfer adjacent to an inclined porous plate embedded in a saturated homogenous porous medium. Heat generation/absorption effects are included. Rosseland's diffusion approximation is used to describe the radiative heat flux in the energy equation. A Darcy model is employed to simulate drag effects in the porous medium. The governing transport equations are rendered into non-dimensional form under the assumption of low Reynolds number and also low magnetic Reynolds number. Using a Galerkin formulation with a weighted residual scheme, finite element solutions are presented to the boundary value problem. The influence of plate inclination, Eringen coupling number, radiation-conduction number, heat absorption/generation parameter, chemical reaction parameter, plate moving velocity parameter, magnetic parameter, thermal Grashof number, species (solutal) Grashof number, permeability parameter, Eckert number on linear velocity, micro-rotation, temperature and concentration profiles. Furthermore, the influence of selected thermo-physical parameters on friction factor, surface heat transfer and mass transfer rate is also tabulated. The finite element solutions are verified with solutions from several limiting cases in the literature. Interesting features in the flow are identified and interpreted.

Keywords : *Heat source/sink*, *chemical reaction, inclined porous plate, micropolar fluid, FEM; radiative heat transfer; thermal convection; viscous heating; materials processing.*

PACS No. : 47.11. Fg, 47.11. +j, 47.50. +d, 44.30. +v

1.Introduction

Non-Newtonian fluid flows feature widely in an extensive range of technological applications including plastic fabrication, food processing, biotechnology and paint emulsion manufacture. To simulate the complex shear stress-strain characteristics of such fluids, numerous mathematical models have been developed. These include viscoelastic and viscoplastic formulations. While these models capture certain physical characteristics of specific materials, they ignore microstructural characteristics. Eringen [1] introduced the *microfluid model* and later simplified this model to micropolar fluids which can describe sophisticated phenomena including couple stresses, body couples and exhibit gyratory motions, which cannot be analyzed with simpler non-Newtonian models. By generalizing of micropolar fluids to heat conduction and other thermal effects, Eringen [2] developed a comprehensive theory for thermo-micropolar fluids. Many recent aspects of micropolar hydrodynamics are documented in Eringen [3] and Lukaswiascz [4]. Extensive discussion of other applications in chemical and mechanical engineering are available in the articles of Airman *et al*. [5, 6]. An important area in which micropolar fluid theory provides deeper insight of fluid dynamic behavior is materials processing. Other applications of thermal (heat transfer) problems are considered in [7-11].

The heat transfer coefficient or thermal boundary condition (s) become an integral part of solving such problems which deviate from the conventional boundary layer flow analysis, in which they are usually specified. This condition is necessary in the heat transfer analysis of extended surfaces where the thermal boundary conditions are specified only at the ends of the surfaces. It may be noted that convective thermal boundary conditions are known to arise in many diverse areas of technology including combustion in gas turbines, convective flows wherein the bounding surfaces absorb heat by solar radiation, design of efficient heat exchangers, optimization of turbine blade cooling system, photovoltaic panels etc. These systems are increasingly deploying or already feature more complex transport fluids containing suspensions. *Micropolar fluid mechanics* therefore offers a robust framework for simulating the non-Newtonian microstructural thermo-fluid characteristics of these technologies. Many investigators have examined boundary value problems of such fluids in recent years using a range of computational solvers. An important analysis in this regard was presented by Abo-Eldahab and Ghonaim [12] who addressed thermal radiation effects

in heat transfer of a micropolar fluid through a porous medium. Hydromagnetic convection heat transfer in a micropolar fluid over a vertical plate was studied by Ferdows *et al.* [13]. Olajuwon and Oahimire [14] obtained perturbation solutions for the double-diffusive convection in *time-dependent* radiative hydromagnetic micropolar convection. Kundu *et al*. [15] studied thermo-diffusive and radiative effects on rotating micropolar convection flows. Rahman and Sultana [16] analyzed magnetic body force and radiative heat transfer effects on micropolar flow with variable heat flux in a porous medium. In case of horizontal and vertical plates convective boundary layer flows have recieved considerable attention. However boundary layer flows adjacent to inclined plates have been studied less frequently for *micropolar flows.* Most studies have been confined to Newtonian flows. Cheng [17] examined the convective flow from an inclined surface through a porous medium. Heat and mass transfer in magneto-convective boundary layer flow from an inclined plate with viscous dissipation in porous media was analyzed by Singh [18]. Sudheer Babu *et al.,* [19] described the effects of mass transfer on unsteady magneto-convection flow of micropolar fluid along a vertical moving porous plate through porous medium with viscous dissipation. Radiation and mass transfer effects on MHD free convective flow of a micropolar fluid from an infinite vertical porous moving plate embedded in a porous medium with viscous dissipation was studied by Roja *et al.* [20]. Chen [21] described the effects of heat and mass transfer in magnetic free convection with Ohmic heating and viscous dissipation. Several studies have examined convection and conduction heat transfer in micropolar flows along inclined surfaces and these include the works of Aurangzaib *et al.* [22] who considered a stretching plate and Srinivas *et al.* [23] who focused on entropy generation aspects.

In the above investigations, the combined effects of *heat source* or *sink* and *chemical reaction* in hydromagnetic micropolar transport have been excluded. However, in many industrial processes e.g. materials fabrication of powders, heat source/sink and chemical reaction effects may exert an influential role. Other applications include heat removal from nuclear fuel debris (solidified melt distributed among fuel assemblies), exothermic chemical reaction and dissociating fluids in PBRs *(packed bed reactors)* and cooling of finned heat sinks [24]. Nayak and Dash [25] studied heat transfer effects on transient mixed radiative convection hydromagnetic flow of a micropolar fluid from a moving semi-infinite vertical porous plate with heat sink and time dependent suction. Khedr *et al.* [26] investigated theoretically the magneto-micropolar convection from a stretched permeable

surface with heat generation or absorption. Further studies of *reactive micropolar flows* include, Magyari and Chamkha [27], Chamkha and Khaled [28] and Rahman *et al.* [29]. In numerous process engineering systems, *chemical reactions* take place, which may be destructive or constructive in nature and can influence significantly heat and mass diffusion phenomena. Generally, boundary layer flow models utilize first order chemical reaction effects and assume the reaction to be destructive. Recently Srinivasacharya and Upender [30] have considered the composite effects of thermal radiation and chemical reaction on magnetic free convection heat and mass transfer in micropolar fluids. Sheri and Shamshuddin [31] have presented numerical solutions for coupled heat and mass transfer in magnetohydrodynamic micropolar flow with both viscous dissipation and chemical reaction effects. Sheri and Shamshuddin [32] have further presented finite element numerical solutions for diffuso-thermal and chemical reaction effects on transient free convection micropolar flow. Further studies of *reactive micropolar flows* include Rawat *et al*. [33] (which considered double diffusive convection in reactive micropolar flow from an extending sheet), Das [34] (who examined slip effects in micropolar fluid over an inclined plate), Pal and Talukdar [35] and also Srinivasacharya [36].

In the present article, motivated by simulating *non-Newtonian thermal materials processing flow*, we have extended the analytical work of Sudheer Babu *et al.* [19] by taking into account of *thermal radiation, heat source/sink and first order chemical reaction effects* and deriving finite element numerical solutions for *generalized micropolar radiative-convection flow from an inclined surface in a porous medium*. The perturbation method approximation solutions presented by Sudheer Babu *et al*. [19] provide a benchmark for the present finite element computational solutions. The effects of various emerging thermo-physical parameters on the velocity, micro-rotation (angular) velocity, temperature and concentration profiles as well as on local skin friction coefficient and wall couple stress are visualized and tabulated. The current problem, to the best knowledge of the authors, has not been communicated thusfar in the technical literature, and provides a deeper insight into more complex rheological high-temperature materials processing operations in which collective effects of magnetohydrodynamics, thermal radiation, non-Newtonian fluid characteristics and filtration media all contribute.

2. Mathematical Model

Free convective flow of an electrically conducting incompressible micropolar fluid from an inclined plane (with inclination angle α to the vertical) is considered. The plane considered is permeable and is moving with constant velocity Up in a porous medium. The physical configuration is illustrated in **Fig. 1**. The inclination angles 0^o,90^o and $0^o \le \alpha \le 90^o$ represent the vertical, horizontal and inclined plate scenarios respectively. Darcy's law is assumed which is valid for low Reynolds number flow (viscous-dominated). A magnetic field of uniform strength B_0 is applied in a direction parallel to the y' axis which is perpendicular to the flow direction. It is assumed that the induced magnetic field is negligible in comparison to the applied magnetic field [37]. Magnetic Reynolds number is therefore very small. The magnetohydrodynamic (MHD) body force term is derived from an order of magnitude analysis of the full Navier-Stokes equations. It is also assumed that applied or polarized voltage is neglected so that no energy is added or extracted from the fluid by electrical means. The fluid is considered to be a gray, absorbing-emitting but non-scattering medium and the Rosseland approximation is used to describe the radiative heat flux. The radiative heat flux in the x' direction is considered negligible in comparison with that of y' direction. Both wall temperature and concentration vary with the distance along the plate and they are always greater than their uniform ambient values existing far from the plate surface. Ohmic (Joule) dissipation is ignored. The magnetic micropolar fluid contains a species which is reactive and obeys a first order homogenous chemical reaction. To simplify the formulation of the boundary conditions, we assumed the size of holes in the porous plate is significantly larger than the characteristic microscopic length scale of the micropolar fluid. It is assumed that the plate is infinite in extent and hence all physical quantities depend only on y' and t'.

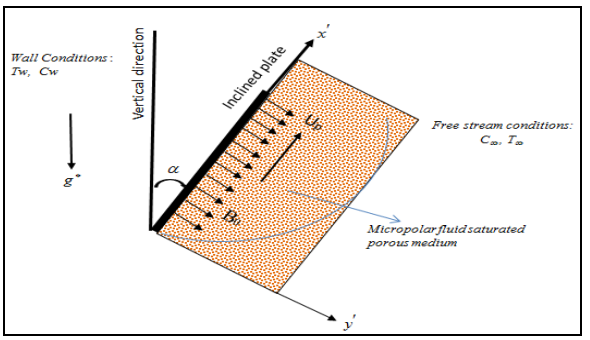

Fig .1: Flow configuration and coordinate system

The Boussinesq approximation is adopted in the momentum equation. The balances of mass, linear momentum, angular momentum, energy, and concentration species in the Cartesian frame are written as follows:

The continuity equation:

$$\frac{\partial v'}{\partial y'} = 0 \tag{1}$$

The momentum equation:

$$\frac{\partial u'}{\partial t'} + v'\frac{\partial u'}{\partial y'} = \left(\nu + \nu_r\right)\frac{\partial^2 u'}{\partial y'^2} + g'\beta_T\left(T'_w - T_\infty\right)Cos(\alpha) + g'\beta_C\left(C'_w - C_\infty\right)Cos(\alpha) - \frac{\nu\, u'}{k} - \frac{\sigma\, B_0^2\, u'}{\rho} + 2\nu_r\frac{\partial \omega'}{\partial y'} \tag{2}$$

The angular momentum equation:

$$\left(\frac{\partial \omega'}{\partial t'} + v'\frac{\partial \omega'}{\partial y'}\right) = \frac{\gamma'}{\rho\, j'}\frac{\partial^2 \omega'}{\partial y'^2} \tag{3}$$

The energy equation:

$$\frac{\partial T'}{\partial t'} + v'\frac{\partial T'}{\partial y'} = \frac{\kappa}{\rho C_p}\left(\frac{\partial^2 T'}{\partial y'^2}\right) - \frac{1}{\rho C_p}\left(\frac{\partial q_r}{\partial y'}\right) + \frac{Q'}{\rho C_p}\left(T'_w - T'_\infty\right) + \frac{\mu}{\rho C_p}\left(\frac{\partial u'}{\partial y'}\right)^2 \tag{4}$$

The concentration equation:

$$\frac{\partial C'}{\partial t'} + v'\frac{\partial C'}{\partial y'} = D_m\left(\frac{\partial^2 C'}{\partial y'^2}\right) - K'_c\left(C'_w - C_\infty\right) \tag{5}$$

Here u' and v' are the velocity components in x' and y' axis respectively. ω' is the micro-rotation component, ν is the kinematic viscosity, ν_r is the kinematic micro-rotation viscosity, ρ is the constant fluid density, σ is the electrical conductivity of the micropolar fluid, g' is the acceleration due to gravity, $\beta_T\left(T'_w - T_\infty\right)$ and $\beta_C\left(C'_w - C_\infty\right)$ denote the thermal and concentration buoyancy effects respectively, B_0 is the strength of the transverse magnetic field, Cp is the specific heat at constant pressure, k is the permeability of the porous medium, D_m is the molecular diffusivity of species and $K'c$ is the dimensional chemical reaction rate constant. Implicit in the present analysis is the assumption of a constant permeable plate velocity in the direction of the fluid flow. The

appropriate initial and boundary conditions for velocity, angular velocity (micro-rotation), temperature and concentrations fields are specified thus:

$$\begin{array}{ll} t' \le 0 & \left\{ u' = 0,\ \omega' = 0,\ T' = T'_{\infty},\ \ C' = C'_{\infty} \qquad \text{for all } y' \ge 0 \right\} \\ t' > 0 & \left\{ \begin{array}{l} u' = u'_P, \omega' = -\dfrac{\partial u'}{\partial y'}, T' = T'_W + \varepsilon\left(T'_W - T'_{\infty}\right)e^{n't'}, C' = C'_W + \varepsilon\left(C'_W - C'_{\infty}\right)e^{n't'} \ \text{at } y' = 0 \\ u' \to 0,\ \omega' \to 0,\ T' \to T'_{\infty},\ C' \to C'_{\infty} \qquad \text{as } y' \to \infty \end{array} \right\} \end{array} \tag{6}$$

Where u'_p is plate velocity, it is clear from the equation of continuity that suction velocity normal to the plate is either a constant or a function of time. Hence it is assumed that the suction velocity takes the form:

$$u' = -V_0 \tag{7}$$

Where V_0 is a scale of suction velocity and $V_0 > 0$. The negative sign indicates that the suction velocity is directed towards the plate. The radiative heat flux term is given by:

$$q_r = \frac{-4\bar{\sigma}}{3\bar{k}}\frac{\partial T'^4}{\partial y'} \tag{8}$$

Here $\bar{\sigma}$ and $\bar{k}$ are the Stefan-Boltzmann constant and mean absorption coefficient, respectively. The assumed Rosseland model has been shown to be generally valid for optically-thick fluid media, as considered in viscous fluids [38]. Implementing eqn. (8) results in a highly nonlinear energy equation in T and it is difficult to obtain a solution. However, researchers have resolved this problem by assuming small temperature differences within the fluid flow (see [39]- [41]). In this situation, Rosseland's model can be linearized about ambient an temperature T'_{∞} assuming that the difference in the temperature within the flow is such that T'^4 can be expressed as a linear combination of the temperature. Using Taylor's series expansion about T' the expansion of T'^4 can be written as follows, neglecting higher order terms:

$$T'^4 = T'^4_{\infty} + 4T'^3_{\infty}\left(T' - T'_{\infty}\right) + 6T'^2_{\infty}\left(T' - T'_{\infty}\right)^2 + \ldots \tag{9}$$

Neglecting higher order terms beyond the first degree in $\left(T' - T'_{\infty}\right)$, we have:

$$T'^4 \cong 4T'^3_{\infty}T - 3T'^4_{\infty} \tag{10}$$

Differentiating equation (8) w.r.t y' and using (10), we obtain:

$$\frac{\partial q_r}{\partial y'} = -\frac{16\, T_\infty'^3\, \bar{\sigma}}{3\,\bar{k}}\left(\frac{\partial^2 T}{\partial y'^2}\right) \tag{11}$$

Now simply replacing T'^3 in Eq. (8) with $T_\infty'^3$, Eq. (4) can be expressed as follows:

$$\left(\frac{\partial T'}{\partial t'} + v'\frac{\partial T'}{\partial y'}\right) = \frac{\kappa}{\rho C_p}\left(1 + \frac{16\bar{\sigma}}{3\bar{k}\,\kappa}T_\infty'^3\right)\frac{\partial^2 T}{\partial y'^2} + \frac{Q'}{\rho C_p}\left(T_w' - T_\infty'\right) + \frac{\mu}{\rho C_p}\left(\frac{\partial u'}{\partial y'}\right)^2 \tag{12}$$

In order to write the governing equations and boundary conditions in dimensionless form, the following non-dimensional quantities are introduced:

$$\left.\begin{aligned} &u = \frac{u'}{U_0},\ v = \frac{v'}{V_0},\ y = \frac{V_0\, y'}{\nu},\ U_p = \frac{u_p'}{U_0},\ n = \frac{n'\nu}{V_o^2},\ \omega = \frac{\nu}{U_0 V_0}\omega', \\ &t = \frac{t' V_0^2}{\nu},\ \theta = \frac{T' - T_\infty'}{T_w' - T_\infty'},\ \phi = \frac{C' - C_\infty'}{C_w' - C_\infty'},\quad j = \frac{V_0^2}{\nu^2}\, j' \end{aligned}\right\} \tag{13}$$

Here U_o represents free stream velocity. Furthermore, the spin gradient viscosity γ' which provides an important relationship between the coefficient of viscosity and microinertia is defined as follows

$$\gamma' = \left(\mu + \frac{\Lambda}{2}\right) j' = \mu\, j'\left(1 + \frac{\beta}{2}\right) \quad where \quad \beta = \frac{\Lambda}{\mu} \tag{14}$$

Here all quantities with a prime are dimensionless. Also θ is dimensionless temperature function, ϕ is dimensionless concentration and β is the Eringen micropolar vortex viscosity parameter. In view of Eqs (6)- (14), the governing equations (2)- (5), after dropping primes, emerge as a system of coupled dimensionless partial differential equations:

$$\frac{\partial u}{\partial t} - \frac{\partial u}{\partial y} = \left(1 + \beta\right)\frac{\partial^2 u}{\partial y^2} + \left(Gr\ \theta + Gc\ \phi\right) Cos\alpha - N\ u + 2\beta\left(\frac{\partial \omega}{\partial y}\right) \tag{15}$$

$$\frac{\partial \omega}{\partial t} - \frac{\partial \omega}{\partial y} = \frac{1}{\eta}\left(\frac{\partial^2 \omega}{\partial y^2}\right) \tag{16}$$

$$\frac{\partial \theta}{\partial t} - \frac{\partial \theta}{\partial y} = \frac{1}{\Gamma}\frac{\partial^2 \theta}{\partial y^2} + H\theta + Ec\left(\frac{\partial u}{\partial y}\right)^2 \tag{17}$$

$$\frac{\partial \phi}{\partial t} - \frac{\partial \phi}{\partial y} = \frac{1}{Sc}\left(\frac{\partial^2 \phi}{\partial y^2}\right) - \gamma\,\phi \tag{18}$$

Where $\eta = \frac{\mu\, j'}{\gamma'} = \frac{2}{2+\beta}$, is the dimensionless micropolar gyro-viscosity material parameter $\Gamma = \left(1 - \frac{4}{3R+4}\right) Pr$, $N = \left(M + \frac{1}{K}\right)$. Also $M = \frac{\sigma\, B_o^2 \nu}{\rho\, V_0^{\,2}}$, is the magnetic field parameter, $K = \frac{V_o^2\, K'}{\nu^2}$ is the permeability parameter for the porous medium, $Pr = \frac{\nu\, \rho\, Cp}{\kappa} = \frac{\mu Cp}{\kappa}$, $Sc = \frac{\nu}{Dm}$, $G_r = \frac{\nu\beta_T g'(T'_w - T'_\infty)}{U_0 V_0^2}$ and $G_c = \frac{\nu\beta_C g'\left(C'_w - C'_\infty\right)}{U_0 V_0^2}$, are Prandtl number, Schmidt number, thermal Grashof and species Grashof number, respectively, $R16\sigma^*\, T_\infty^3 / 3k\, k^*$, is thermal radiation-conduction parameter, $H = Q^*\, \nu / \rho\, Cp V_o^{\,2}$ is heat source/sink parameter, $E_c = V_0^2 / C_p\left(T'_w - T'_\infty\right)$ is the Eckert number, $\gamma = K'_c\, \nu / V_0^2$ is homogeneous chemical reaction parameter and $\beta = \Lambda / \mu$ is the Eringen coupling number (vortex viscosity ratio parameter). The boundary conditions can be written in non-dimensional form as follows:

$$t \le 0 \;:\; \left\{ u = 0,\ \omega = 0, T = T_\infty,\ C = C_\infty \qquad for\ \ all\ \ y \ge 0 \right\}$$

$$t > 0 \;:\; \left\{ \begin{array}{lll} u = U_p, & \omega = -\frac{\partial u}{\partial y}, \quad \theta = 1 + \varepsilon e^{nt}\ , \quad \phi = 1 + \varepsilon e^{nt} & at\ \ y = 0 \\ u \to 0, & \omega \to 0, \quad \theta \to 0, \quad \phi \to 0 & as\ y \to \infty \end{array} \right\} \qquad (19)$$

The mathematical statement of the problem is now complete and embodies the solution of Eqs. (15)- (18) with modified boundary conditions (19). The system is well-posed. The skin friction coefficient and couple stress coefficient are important parameters for this type of boundary layer flow and frequently used in materials processing simulations and design.

The skin-friction at the plate in *non-dimensional* form is given by:

$$C_f = \left(\frac{\partial u}{\partial y}\right)_{y=0} \qquad (20)$$

The couple stress coefficient at the plate in *non-dimensional* form is given by:

$$C_m = \left(\frac{\partial \omega}{\partial y}\right)_{y=0} \qquad (21)$$

Nusselt number is computed in *non-dimensional* form as:

$$Nu / Re_x = -\left[\frac{\partial \theta}{\partial y}\right]_{y=0} \tag{22}$$

Sherwood number is evaluated as in *non-dimensional* form by:

$$Sh / Re_x = -\left[\frac{\partial \phi}{\partial y}\right]_{y=0} \tag{23}$$

Here $Re_x = \frac{V_o x}{\nu}$ is the *local Reynolds number* based on the plate suction velocity.

3. Finite Element Method Numerical Solution

The finite element method (FEM) is employed to solve the transformed, coupled boundary value problem defined by eqns. (15) -(18) under (19). FEM is the most popular and adaptable method available to engineers. The general details of the *variational* finite element method are described at length in Rao [42] and Reddy [43]. FEM has been applied to study many transport problems of micropolar fluids and magnetic liquids and relevant references in this regard are [44-47]. The fundamental steps involved in the finite-element analysis of a problem are as follows:

- *Discretization of the infinite fluid domain into finite elements*
- *Derivation of element equations*
- *Assembly of element equations*
- *Imposition of boundary conditions*
- *Solution of assembled equations*

The final matrix equation obtained can be solved by any efficient iterative scheme.

3.1 Variational formulation

The variational formulation associated with Eqns. (15) - (18) over a *typical two-node linear element* $\left(y_e,\ y_{e+1}\right)$ is given by:

$$\int_{y_e}^{y_{e+1}} w_1\left[\frac{\partial u}{\partial t} - \left(\frac{\partial u}{\partial y}\right) - A_1\left(\frac{\partial^2 u}{\partial y^2}\right) - (Gr\theta + Gc\phi)\cos\alpha - N(u) - A_2\left(\frac{\partial \omega}{\partial y}\right)\right] dy = 0 \tag{24}$$

$$\int_{y_e}^{y_{e+1}} w_2\left[\frac{\partial \omega}{\partial t} - \left(\frac{\partial \omega}{\partial y}\right) - \frac{1}{\eta}\left(\frac{\partial^2 \omega}{\partial y^2}\right)\right] dy = 0 \tag{25}$$

$$\int_{y_e}^{y_{e+1}} w_3\left[\frac{\partial \theta}{\partial t} - \left(\frac{\partial \theta}{\partial y}\right) - A_3\left(\frac{\partial^2 \theta}{\partial y^2}\right) + H\theta - Ec\left(\frac{\partial u}{\partial y}\right)^2\right] dy = 0 \tag{26}$$

$$\int_{y_e}^{y_{e+1}} w_4\left[\frac{\partial \phi}{\partial t}-\left(\frac{\partial \phi}{\partial y}\right)-\frac{1}{Sc}\left(\frac{\partial^2 \phi}{\partial y^2}\right)+\gamma\,\phi\right]dy=0 \tag{27}$$

Where $A_1 = 1+\beta$, $A_2 = (2\beta)$, $A_3 = \frac{1}{\Gamma}$ and w_1, w_2, w_3, w_4 are arbitrary test functions and may be viewed as the variations in u, ω , θ and ϕ respectively. After dropping the order of integration and non-linearity, we arrive at the following system of equations:

$$\int_{y_e}^{y_{e+1}} \left[\begin{array}{l}(w_1)\frac{\partial u}{\partial t}-(w_1)\frac{\partial u}{\partial y}+A_1\frac{\partial w_1}{\partial y}\frac{\partial u}{\partial y}+N(w_1)u-\left[Gr\,(w_1)\theta+Gc(w_1)\phi\right]\cos\alpha \\ -A_2(w_1)\frac{\partial \omega}{\partial y}\end{array}\right]dy-\left[w_1\left(\frac{\partial u}{\partial y}\right)\right]_{y_e}^{y_{e+1}}=0 \tag{28}$$

$$\int_{y_e}^{y_{e+1}}\left[(w_2)\frac{\partial \omega}{\partial t}-(w_2)\frac{\partial \omega}{\partial y}+\frac{1}{\eta}\left(\frac{\partial w_2}{\partial y}\right)\left(\frac{\partial \omega}{\partial y}\right)\right]dy-\left[(w_2)\left(\frac{\partial \omega}{\partial y}\right)\right]_{y_e}^{y_{e+1}}=0 \tag{29}$$

$$\int_{y_e}^{y_{e+1}}\left[(w_3)\frac{\partial \theta}{\partial t}-(w_3)\frac{\partial \theta}{\partial y}+A_3\left(\frac{\partial w_3}{\partial y}\right)\left(\frac{\partial \theta}{\partial y}\right)+H(w_3)\theta-Ec\,(w_3)\left(\frac{\partial \bar{u}}{\partial y}\right)\left(\frac{\partial u}{\partial y}\right)\right]dy-\left[A_3(w_3)\left(\frac{\partial \theta}{\partial y}\right)\right]_{y_e}^{y_{e+1}}=0 \tag{30}$$

$$\int_{y_e}^{y_{e+1}}\left[(w_4)\frac{\partial \phi}{\partial t}-(w_4)\left(\frac{\partial \phi}{\partial y}\right)+\frac{1}{Sc}\left(\frac{\partial w_4}{\partial y}\right)\left(\frac{\partial \phi}{\partial y}\right)+\gamma\,(w_4)\,\phi\right]dy-\left[\frac{(w_4)}{Sc}\left(\frac{\partial \phi}{\partial y}\right)\right]_{y_e}^{y_{e+1}}=0 \tag{31}$$

3.2 Finite Element formulation

The finite element model may be obtained from Eqs. (28) - (31) by substituting *finite element approximations* of the form:

$$u=\sum_{j=1}^{2}u_j^e\psi_j^e,\ \omega=\sum_{j=1}^{2}\omega_j^e\psi_j^e,\ \theta=\sum_{j=1}^{2}\theta_j^e\psi_j^e \text{ and } \phi=\sum_{j=1}^{2}\phi_j^e\psi_j^e \tag{32}$$

With $w_1 = w_2 = w_3 = w_4 = \psi_j^e\ (i=1,2)$, where u_j^e , ω_j^e ,θ_j^e and ϕ_j^e are the velocity in the direction of *x*-axis, *y*-axis and temperature respectively at the j^{th} node of typical e^{th} element (y_e, y_{e+1}) and ψ_i^e are the shape functions for this element (y_e, y_{e+1}) and are taken as:

$$\psi_1^e=\frac{y_{e+1}-y}{y_{e+1}-y_e} \text{ and } \psi_2^e=\frac{y-y_e}{y_{e+1}-y_e},\ y_e\le y\le y_{e+1} \tag{33}$$

The finite element model of the equations for the e^{th} element thus formed is given by.

$$\begin{bmatrix} [K^{11}] & [K^{12}] & [K^{13}] & [K^{14}] \\ [K^{21}] & [K^{22}] & [K^{23}] & [K^{24}] \\ [K^{31}] & [K^{32}] & [K^{33}] & [K^{34}] \\ [K^{41}] & [K^{42}] & [K^{43}] & [K^{44}] \end{bmatrix} \begin{bmatrix} \{U^e\} \\ \{\omega^e\} \\ \{\theta^e\} \\ \{\phi^e\} \end{bmatrix} + \begin{bmatrix} [M^{11}] & [M^{12}] & [M^{13}] & [M^{14}] \\ [M^{21}] & [M^{22}] & [M^{23}] & [M^{24}] \\ [M^{31}] & [M^{32}] & [M^{33}] & [M^{34}] \\ [M^{41}] & [M^{42}] & [M^{43}] & [M^{44}] \end{bmatrix} \begin{bmatrix} \{U'^e\} \\ \{\omega'^e\} \\ \{\theta'^e\} \\ \{\phi'^e\} \end{bmatrix} = \begin{bmatrix} \{b^{1e}\} \\ \{b^{2e}\} \\ \{b^{3e}\} \\ \{b^{4e}\} \end{bmatrix} \tag{34}$$

Where $\{[K^{mn}],[M^{mn}]\}$ and $\{\{u^e\},\{\omega^e\},\{\theta^e\},\{\phi^e\},\{u'^e\},\{\omega'^e\},\{\theta'^e\},\{\phi'^e\}$ and $\{b^{me}\}\}$ $(m,n=1,\ ,2,3,4)$ are the set of matrices of order 2×2 and 2×1 respectively and $prime\ (')$ indicates $\frac{d}{dy}$. These matrices are defined as follows:

$$\begin{cases} K_{ij}^{11} = -\int_{y_e}^{y_{e+1}} \left[(\psi_i^e) \left(\frac{\partial \psi_j^e}{\partial y} \right) \right] dy + A_1 \int_{y_e}^{y_{e+1}} \left[\left(\frac{\partial \psi_i^e}{\partial y} \right) \left(\frac{\partial \psi_j^e}{\partial y} \right) \right] dy, \\ K_{ij}^{12} = N \int_{y_e}^{y_{e+1}} (\psi_i^e)(\psi_j^e) dy, \\ K_{ij}^{13} = -A_2 \int_{y_e}^{y_{e+1}} \left[(\psi_i^e) \left(\frac{\partial \psi_j^e}{\partial y} \right) \right] dy, \\ K_{ij}^{14} = -[Gr + Gc] Cos\alpha \int_{y_e}^{y_{e+1}} (\psi_i^e)(\psi_j^e) dy, \\ M_{ij}^{11} = \int_{z_e}^{z_{e+1}} (\psi_i^e)(\psi_j^e) dy,\ M_{ij}^{12} = M_{ij}^{13} = M_{ij}^{14} = 0 \end{cases} \tag{35}$$

$$\begin{cases} K_{ij}^{21} = -\int_{y_e}^{y_{e+1}} \left[(\psi_i^e) \left(\frac{\partial \psi_j^e}{\partial y} \right) \right] dy, \\ K_{ij}^{22} = -\frac{1}{\eta} \int_{y_e}^{y_{e+1}} \left[\left(\frac{\partial \psi_i^e}{\partial y} \right) \left(\frac{\partial \psi_j^e}{\partial y} \right) \right] dy, \\ K_{ij}^{23} = 0,\ K_{ij}^{24} = 0 \\ M_{ij}^{21} = M_{ij}^{22} = 0, M_{ij}^{23} = \int_{y_e}^{y_{e+1}} (\psi_i^e)(\psi_j^e) dy,\ M_{ij}^{24} = 0, \end{cases} \tag{36}$$

$$\begin{cases} K_{ij}^{31} = -Ec \int_{y_e}^{y_{e+1}} (\psi_i^e) \left(\frac{\partial \bar{u}}{\partial y} \right) \left(\frac{\partial \psi_j^e}{\partial y} \right) dy, \\ K_{ij}^{32} = -\int_{y_e}^{y_{e+1}} \left[(\psi_i^e) \left(\frac{\partial \psi_j^e}{\partial y} \right) \right] dy + A_3 \int_{y_e}^{y_{e+1}} \left[\left(\frac{\partial \psi_i^e}{\partial y} \right) \left(\frac{\partial \psi_j^e}{\partial y} \right) \right] dy, \\ K_{ij}^{33} = H \int_{y_e}^{y_{e+1}} [\psi_i^e] dy,\ K_{ij}^{34} = 0, \\ M_{ij}^{31} = 0, M_{ij}^{32} = 0, M_{ij}^{33} = \int_{y_e}^{y_{e+1}} (\psi_i^e)(\psi_j^e) dy,\ M_{ij}^{34} = 0 \end{cases} \tag{37}$$

$$\begin{cases} K_{ij}^{41}=0, \\ K_{ij}^{42}=-\int_{y_e}^{y_{e+1}}\left[\left(\psi_i^e\right)\left(\frac{\partial \psi_j^e}{\partial y}\right)\right]dy+\frac{1}{Sc}\int_{y_e}^{y_{e+1}}\left[\left(\frac{\partial \psi_i^e}{\partial y}\right)\left(\frac{\partial \psi_j^e}{\partial y}\right)\right]dy, \\ K_{ij}^{43}=\gamma\int_{y_e}^{y_{e+1}}\left(\psi_i^e\right)\left(\psi_j^e\right)dy,\ K_{ij}^{44}=0, \\ M_{ij}^{41}=0,\ M_{ij}^{42}=0,\ M_{ij}^{43}=\int_{y_e}^{y_{e+1}}\left(\psi_i^e\right)\left(\psi_j^e\right)dy,\ M_{ij}^{44}=0 \end{cases} \tag{38}$$

$$\begin{cases} b_i^{1e}=\left[\left(\psi_i^e\right)\left(\frac{\partial u}{\partial y}\right)\right]_{y_e}^{y_{e+1}},\ b_i^{2e}=\left[\left(\psi_i^e\right)\left(\frac{\partial \omega}{\partial y}\right)\right]_{y_e}^{y_{e+1}}, \\ b_i^{3e}=\left[A_3\left(\frac{\partial \theta}{\partial y}\right)\right]_{y_e}^{y_{e+1}},\ b_i^{4e}=\left[\frac{\left(\psi_i^e\right)}{Sc}\left(\frac{\partial \phi}{\partial y}\right)\right]_{y_e}^{y_{e+1}} \end{cases} \tag{39}$$

In one-dimensional space, linear and quadratic elements or higher order elements can be deployed. Here the entire flow domain is considered by dividing it into successively sized grids of order 81x81, 101x101 and 121x121 in the *y*-axis direction. After many tests a grid size with 101 intervals has been adopted. Thus, all the computations are executed with 101 intervals of equal step size 0.01. At each node, 4 functions are to be evaluated and after assembly of the element equations, a set of 404 non-linear equations are obtained which necessitate an iterative solution subject to the specified boundary conditions. The iterative process is terminated when the following condition is met: $\sum_{i,j}\left|\xi^{n+1}-\xi^{n}\right|\le 10^{-6}$ where $\xi=u,\omega,\theta$ and ϕ are velocity along x axis, microrotation, temperature and concentration respectively and n denote the iterative step. To see the effects of step size (*h*) the finite element code is run with step sizes as h=0.01 and very good agreement is obtained for different profiles.

Table 1: Effects of β, Gr, Gc *and* M on C_f, C_m, Nu/Re_x *and* Sh/Re_x

β	Gr	Gc	M	C_f	Cm	Nu/Re_x	Sh/Re_x
0.0	2.0	2.0	2.0	3.4848	3.4789	0.5372	0.7113
0.1	2.0	2.0	2.0	0.7551	0.7551	0.5375	0.7113
0.5	2.0	2.0	2.0	0.7097	0.7096	0.5310	0.7113
0.1	**4.0**	2.0	2.0	1.7222	1.7129	0.5345	0.7113
0.1	2.0	**4.0**	2.0	0.7174	0.7115	0.5050	0.7113
0.1	2.0	2.0	**1.0**	1.1444	1.1445	0.5368	0.7113

Table 2: Effects of $Pr, R \ and \ Ec$ on C_f, C_m, Nu / Re_x and Sh / Re_x

Pr	R	Ec	Sc	K	C_f	C_m	Nu / Re_x	Sh / Re_x
0.71	2.0	0.01	0.6	0.5	3.4847	3.7937	0.5372	0.7113
5.0	2.0	0.01	0.6	0.5	0.6873	0.6372	0.6722	0.7113
0.71	**1.0**	0.01	0.6	0.5	0.7845	0.7844	0.4151	0.7113
0.71	2.0	**1.0**	0.6	0.5	0.6181	0.6180	0.7116	0.7113
0.71	2.0	0.01	**0.2**	0.5	0.9494	0.9493	0.5390	0.3109
0.71	2,0	0.01	0.6	**1.5**	1.9591	0.4991	1.0252	1.0252

Table 1 and **Table 2** document the friction factor, surface heat transfer and mass transfer rate dependency on the emerging thermo-physical parameters.

Table 1 depicts the effect of β, Gr, Gc, M on $C_f, C_m, Nu / Re_x, Sh / Re_x$ respectively. It is observed that the skin friction decreases as β, Gc increases while it increases as Gr increases. As M decreases skin friction increases. The same trend is observed in case of wall couple stress. Further, it is observed that the Nusselt number decreases as β, Gr, Gc increases but as M increases, Nusselt number decreases. Sherwood number has no significant effect on β, Gr, Gc, M. **Table 2** depicts the effect of Pr, R, Ec, Sc, K on $C_f, C_m, Nu / Re_x, Sh / Re_x$ respectively. The skin friction coefficient decreases as Pr, Ec, R, K increases, while it decreases as Sc decreases. The same trend is computed in the case of wall couple stress (wall micro-rotation gradient). Further, it is observed that the Nusselt number decreases as R decreases. Nusselt number increases as Sc decreases, while it increases as Pr, Ec, K increases. Sherwood number decreases as Sc decreases and Sherwood number increases as K increases. No tangible modification is computed in Sherwood number (wall mass transfer rate) with a change in Pr, R, Ec. Numerical values of the coefficients proportional to the skin friction C_f, couple stress coefficient C_w, Nusselt number Nu and Sherwood number Sh are given in **Table 3** for the general model with all parameters invoked.

Table 3: Effects of various parameters on C_f, C_m, Nu/Re_x and Sh/Re_x for α, H, δ with $t=1, n=0.1, \varepsilon=0.01, Up=0.5, \beta=0.5, M=2, Gr=2, Gc=2, Pr=0.71, R=2, Ec=0.01$

Parameters	values	C_f	C_m	Nu/Re_x	Sh/Re_x
α	π/4	3.5111	2.0212	0.3542	0.4003
	π/2	3.4561	1.9976	0.3618	0.3911
H	0.5	0.5108	0.5105	0.6121	0.6007
	1.0	0.7389	0.7387	0.4267	0.6007
γ	1.0	2.4215	2.7313	0.5663	1.4615
	2.0	2.3312	2.7215	0.5663	1.4821

It is evident from Table 3, that as angle of inclination (α) and homogeneous chemical reaction parameter (δ) increase, the skin friction coefficient C_f and wall couple stress coefficient C_m *both decrease*. However, with greater heat source/sink parameter (H), the skin friction coefficient C_f and wall couple stress coefficient C_m both increase. Also, it is apparent that as chemical reaction (γ) increases, a significant increase is computed in Sherwood number, Sh. Conversely with increasing angle of inclination, there is a *reduction* in Sherwood number Sh i.e. mass transfer rates at the plate surface are decreased. Furthermore, with an increase in angle of inclination (α), the Nusselt number (Nu) increases i.e. wall heat transfer rates are *enhanced* at the plate surface. Additionally, with an increase in heat source/sink parameter (H), the Nusselt number (Nu) decreases i.e. wall heat transfer rates are *reduced* at the plate surface.

4. Results and Discussion

Herein we present extensive computations in **Figs.2-23** to visualize the influence of key thermo-physical parameters on the unsteady micropolar fluid transport characteristics i.e. translation velocity, angular velocity (micro-rotation), temperature and concentration profiles. In the present study we adopted the following default parameter values for finite element computations i.e. $t=1$, $n=0.1$. While $\beta, M, \alpha, K, Pr, Gr, Gm, Sc, R,$ Ec and δ are varied over a range, which are listed in the figure legends. The permeability in all the figures plotted is set at 0.5 which corresponds to a highly permeable regime as typified by materials fabrication operations. Prandtl

number (*Pr*) is taken to be 0.71 which corresponds to air at 20°C and 1 atmospheric Pressure and the value of Sc is 0.6(water-vapour).

The influence of micro-rotation parameter β on velocity and micro-rotation profiles is illustrated in **Figs. 2-3.** It is seen that as β increases, the velocity gradient near the porous plate decreases, and then approaches to the free stream velocity. Also, it is noteworthy that velocity distribution across the boundary layer is lower for Newtonian fluid (β = 0) as compared with *strongly micropolar fluid* (β = 0.2) for the same conditions and fluid properties. Micropolarity (i.e. increasing vortex viscosity of micro-elements) therefore consistently induces deceleration in the flow adjacent to the plate. All profiles are parabolic and peak at some distance from the wall, decaying smoothly to vanish in the free stream. In addition, the magnitude of microrotation at the wall is decreased as β increases. However, the distribution of microrotation across boundary layer does not show consistent variations with increase of β.

The influence of angle of inclination (α) of the surface on velocity and microrotation profiles has been depicted in **Figs. 4-5**. It is clearly observed from the figures that velocity is decreased with an increase in the angle of inclination of the plate, which implies that greater drag is experienced at the plate surface and the momentum boundary layer thickness is increased (flow deceleration). Furthermore, the buoyancy effects decrease by a factor of gravity body force component, $\cos\alpha$.

Hence the fluid attains higher velocity profiles for the vertical plate $(i.e., \alpha = 0^0)$ than that of inclined plate, while the opposite behavior is observed for micro-rotation i.e. angular velocity. Consequently, as a result of decrease in both thermal and species buoyancy forces arising in the dimensionless momentum eqn. (15) with greater plate inclination, there is a deceleration in the linear flow (increased momentum boundary layer thickness) and acceleration in the angular flow (decreased angular momentum boundary layer thickness). The plate inclination therefore induces a significant modification in both linear and angular velocity (micro-rotation) distributions.

The effect of thermal radiation-conduction parameter (R) on linear velocity and temperature is presented in **Figs. 6-7**. This parameter is defined as $R = 16\bar{\sigma}\, T_\infty^3 / 3k\, \bar{k}$ and features in the

augmented thermal diffusion term in eqn. (17) i.e. $\frac{1}{\Gamma}\frac{\partial^2\theta}{\partial y^2}$. It defines the relative contribution of thermal radiation heat transfer to thermal conduction heat transfer. When $R<1$, thermal conduction dominates. When $R=1$, both thermal conduction and thermal radiation contributions are equal. For $R>1$ thermal radiation dominates over thermal conduction. In the present simulations, we confine attention to the last of these three cases i.e. $R>1$ wherein thermal radiative flux is substantial. Fig. 6 clearly reveals that there is a strong deceleration in the linear velocity with increasing *R* values. The energizing of the flow enhances thermal diffusion but counteracts momentum diffusion. This leads to an increase in momentum boundary layer thickness. A similar observation has been reported by Abo-Eldahab and Ghonaim [12] and Olajuwon and Oahimire [14]. Increasing radiation-conduction parameter is also found to decrease temperatures in the boundary layer (Fig. 7). Thermal boundary layer thickness is therefore also reduced with greater values of R.

Figs. 8-9 shows the graphical representation of the non-dimensional velocity and temperature profiles for some representative values of the temperature dependent and surface dependent heat source (or sink) parameter $H=-2,-1,0,1$. It is to be noted that negative values of H indicate heat source while positive values of H correspond to heat sink. From Fig.8, it is observed that due to heat source $(H>0)$ the buoyancy force increases which in turn manifests in higher velocities in the boundary layer i.e. flow acceleration. On the other hand, when heat sink $(H<0)$ is present, the buoyancy force decreases inducing flow deceleration. For both heat source and sink, the peak velocities occur near the surface of the plate. Fig. 9 depicts heat source/sink effect on temperature and indicates that as H increases from negative to positive values, the temperature as well as thermal boundary layer thickness increases. This is due to fact that the heat source introduces thermal energy to the plate which increases temperature, energizes the boundary layer and elevates thermal boundary layer thickness. For the case of heat sink more heat is removed from the plate which decreases temperature and allows *effective cooling of the boundary layer*. These thermal effects may therefore be exploited to advantage in materials processing systems to control temperatures in manufactured materials which in turn influence other characteristics.

Figs. 10-11 represents the influence of chemical reaction parameter (γ) on the velocity and concentration profiles. The reaction parameter is based on a first-order irreversible chemical reaction which takes place both in the bulk of the fluid (homogeneous) as well as at the plate which is assumed to be catalytic to chemical reaction. Although chemical reactions generally fall into one of two categories i.e. homogenous or heterogenous, the former is of interest in the present study. Homogenous chemical reactions take place uniformly throughout a given phase and exert a similar influence to an *internal source of heat generation*. We consider the destructive type of homogenous chemical reaction. Increasing the chemical reaction parameter γ produces a decrease in velocity. The momentum boundary layer thickness is therefore increased substantially with greater chemical reaction effect. It is noticed that concentration distributions decrease when the chemical reaction increases. Physically, for a destructive case, chemical reaction takes place and progressively destroys the original species. This, in turn, suppresses molecular diffusion of the remaining species which leads to a fall in concentration magnitudes and a decrease in concentration boundary layer thickness.

The profiles of the velocity and microrotation in the boundary layer for various values of the plate moving velocity U_p are shown in **Figures 12 -13** in the direction of the fluid flow. It is noticed that the peak value of velocity across the boundary layer increases near the porous plate as the plate velocity increases. The results also show that the magnitude of microrotation on porous plate decreases as U_p increases. The linear flow is therefore accelerated with greater plate velocity whereas the micro-rotation (angular flow) of micro-elements is inhibited i.e. decelerated.

Figs. 14-15 represents the influence of Grashof number Gr and modified Grashof number Gc on velocity and microrotation profiles. The thermal Grashof number, Gr, quantifies the relative magnitude of the buoyancy force and the opposing frictional (viscous) forces acting on the micropolar fluid. Physically the positive, negative and zero $(i.e.,\ Gr > 0, Gr < 0 \ and \ \ Gr = 0)$ values of the Grashof number correspond to cooling, heating of the boundary surface and absence of free convection currents, respectively. The species (solutal) Grashof number i.e. Gc embodies the relative contribution of species buoyancy force to viscous hydrodynamic force. It is observed that the velocity increases as Gr or Gc increases. Furthermore, the peak value of velocity increases

rapidly near the wall of the porous plate. However, the converse behavior is computed in the case of micro-rotation profiles. Thermal and species buoyancy therefore modify linear and angular velocity fields in a different fashion with different implications for boundary layer thicknesses.

Figs. 16-17 show the pattern of the velocity and microrotation for different values of magnetic field parameter M . It is observed that the amplitude of the velocity as well as the boundary layer thickness decreases when M is increased. Physically, in magnetohydrodynamic materials processing, the applied magnetic field exerts a retarding effect on the free convective flow, transverse to the direction of imposition of the magnetic field. With increasing the values of M , this type of resisting force slows down the fluid i.e. with stronger magnetic field strength the flow is decelerated and this is confirmed with the decreasing velocity distribution across the boundary layer. In case of Fig. 17 an increase in magnetic parameter is observed to significantly accelerate the angular velocity i.e. enhance the magnitude of micro-rotation, although the effect is more localized at the plate surface and progressively grows further from the plate. In both Figs. 16 and 17 asymptotically smooth solutions are obtained indicating that a sufficiently large infinity boundary condition is prescribed in the free stream. Linear momentum boundary layer thickness is therefore increased with greater magnetic parameter whereas angular momentum boundary layer thickness is reduced.

Figs. 18-19 visualize the effect of the porous medium permeability parameter (*K*) on both velocity and microrotation fields. This parameter characterizes the hydraulic transmissivity of the porous medium. It arises in the Darcian drag force term in the composite linear momentum eqn. (16), viz $-(1/K)u$ .With increasing permeability the regime, the quantity of solid fibers progressively decreases. The Darcian bulk impedance to flow is therefore also decreased. This results in acceleration in the velocity u , as observed in Fig. 18. This behaviour is sustained across the boundary layer i.e. for all values of transverse co-ordinate, y . It is also apparent that micro-rotation i.e. angular velocity is *enhanced* with greater permeability parameter although the effect is more prominent near the plate surface and is weakened with further distance into the boundary layer. Since the permeability parameter does not arise in the angular momentum conservation (boundary layer) eqn. (17) the accelerating effect on micro-rotation is sustained via the boost in linear momentum experienced through the *coupling terms* which link both linear and angular momentum

fields. The increase in permeability implies greater void space in the porous medium. This allows an enhancement in gyratory motions as the micro-elements are afforded greater space in which to spin. Similar observations have been reported by Zueco *et al.* [48] and Mohammadein *et al.* [49].

Figs. 20-21 present the effects of the viscous dissipation parameter i.e., the Eckert number Ec on the velocity and temperature fields. Eckert number signifies the quantity of mechanical energy converted via internal friction to thermal energy i.e. heat dissipation. Increasing *Ec* values will therefore cause an increase in thermal energy contributing to the flow and will heat the regime. Positive Eckert number implies cooling of the wall and therefore a transfer of heat to the micropolar fluid. Convection is enhanced and we observe that in consistency with this, the micropolar fluid is accelerated i.e. linear velocity is elevated (Fig. 20). Temperatures are markedly increased with greater Eckert number (Fig. 21). For all non-zero values of *Ec the* temperature overshoot near the wall is distinct; this overshoot migrates marginally further into the boundary layer with an increase in *Ec*. Very smooth decays in temperature profiles are observed for all values of Eckert number and the convergence of profiles in the free stream indicates that an adequately large infinity boundary condition has been imposed in the finite element model.

The velocity and concentration profiles for different values of Schmidt number, *Sc* are illustrated in **Figs. 20-21.** The Schmidt number embodies the ratio of the momentum to the mass diffusivity i.e. $Sc = \nu / D$. The Schmidt number therefore quantifies the relative effectiveness of momentum and mass transport by diffusion in the hydrodynamic (velocity) and concentration (species) boundary layers. For $Sc > 1$ momentum diffusion rate *exceeds* the species diffusion rate. The opposite applies for $Sc < 1$. For $Sc = 1$ both momentum and concentration (species) boundary layers will have the same thickness and diffusivity rates will be equal. It is observed that as the Schmidt number increases velocity decreases. The momentum boundary layer thickness is also reduced with greater Schmidt number. However, it is apparent that species (concentration) profiles gradually increase with higher Schmidt number. Smaller values of Sc are equivalent to increasing the chemical molecular diffusivity and vice versa for larger values of *Sc*.

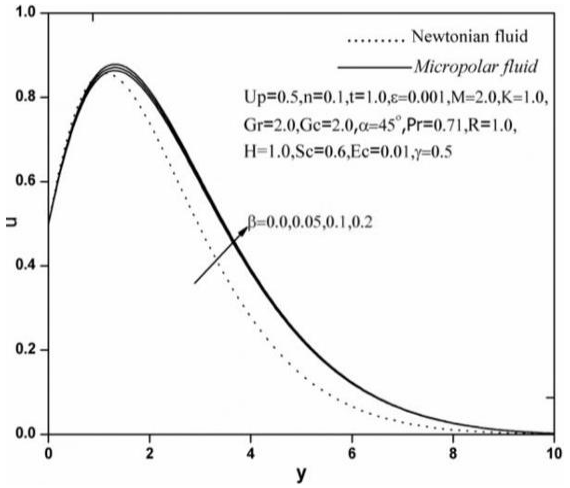

Fig. 2: Velocity profiles for various values of β

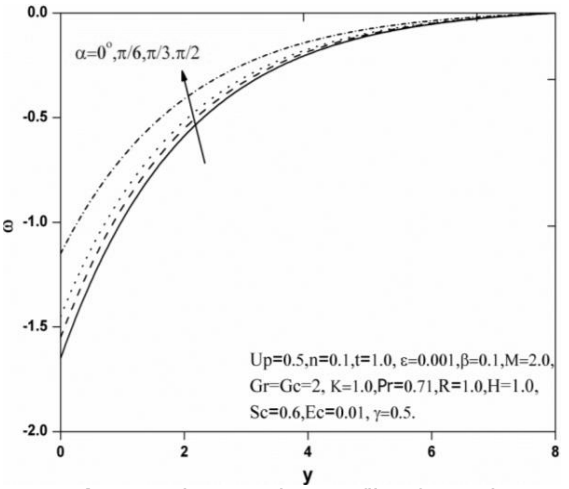

Fig. 5 : Microrotation profiles for various values of α

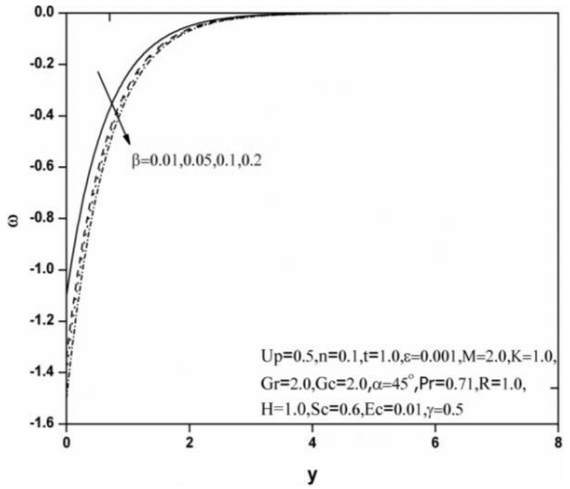

Fig. 3: Micro-rotation profiles for various values of β

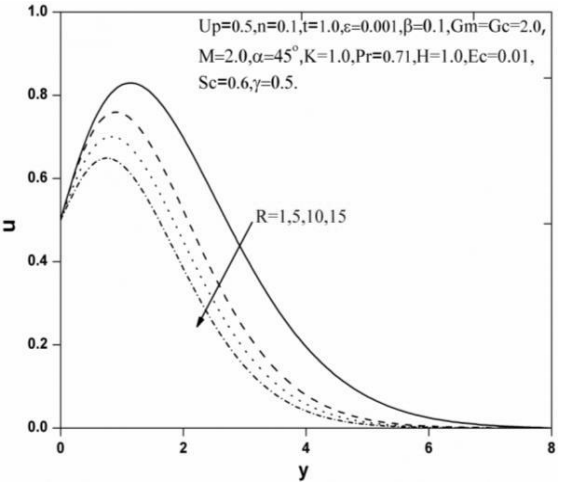

Fig. 6: Velocity profiles for varoius values of R

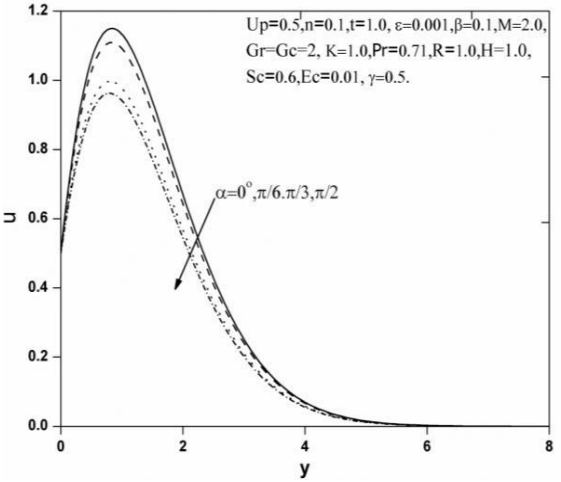

Fig. 4 : Velocity profiles for various values of α

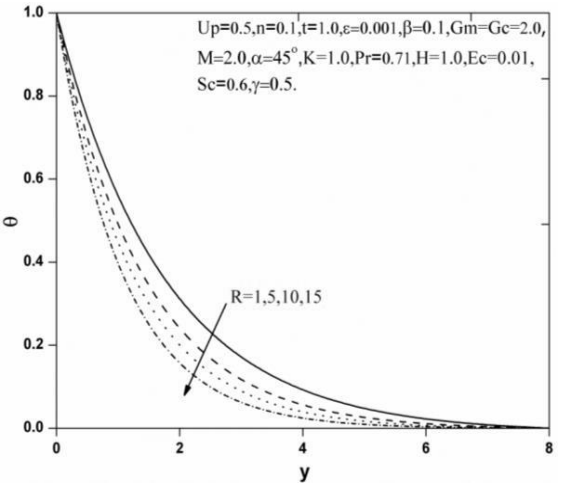

Fig. 7 : Temperature profiles for various values of R

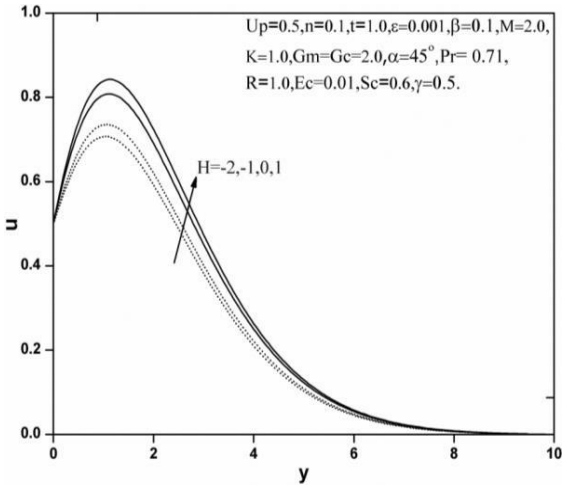

Fig. 8: Velocity profiles for various values of H

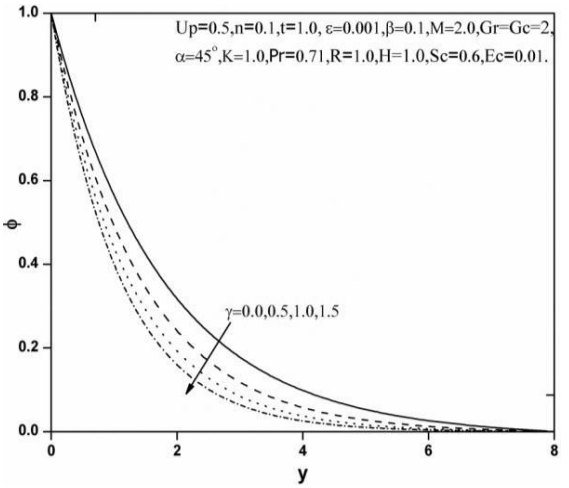

Fig. 11 : Concentration profiles for various values of γ

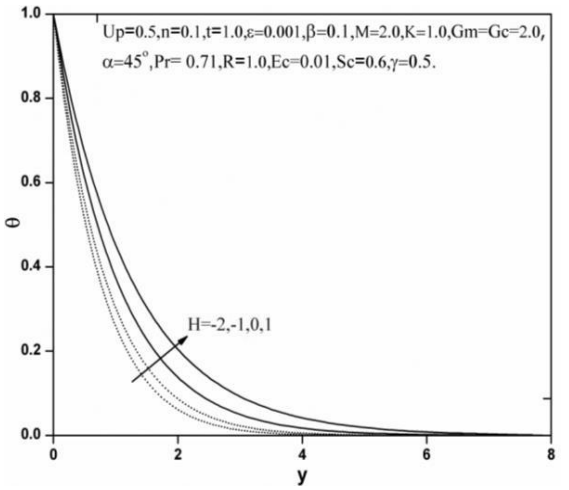

Fig. 9 : Temperature profiles for various values of H

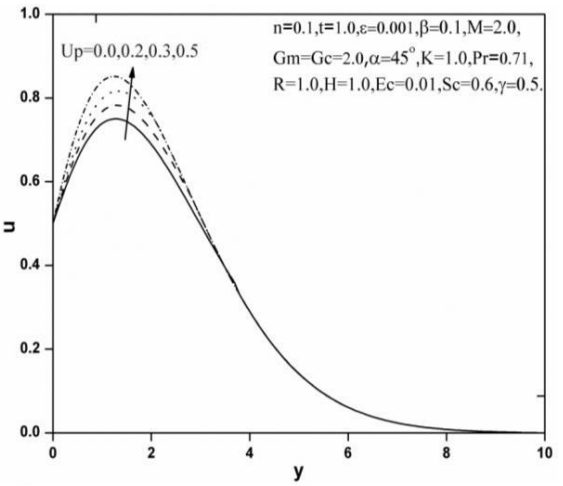

Fig. 12 : Velocity profiles for various values Up

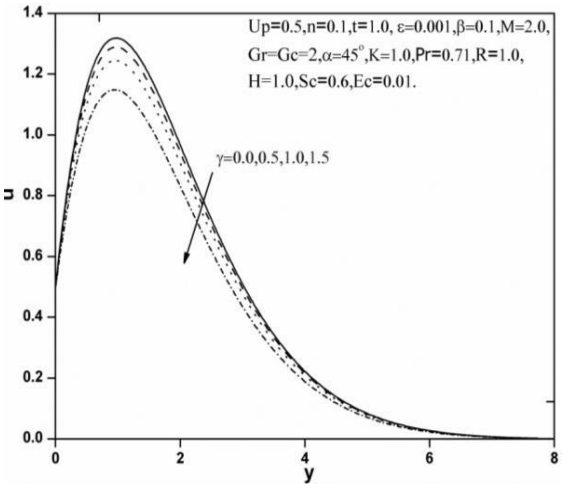

Fig. 10: Velocity profiles for various values of γ

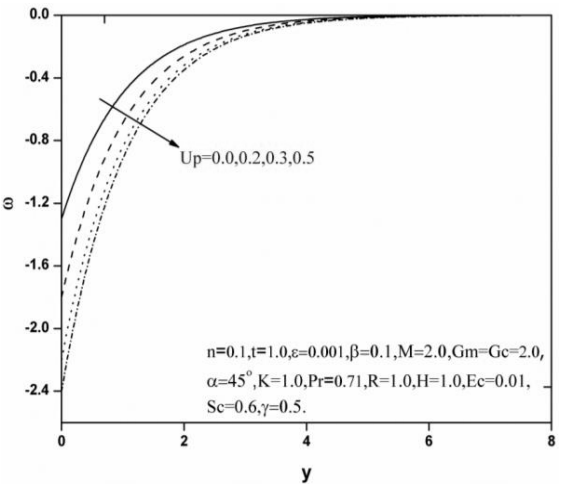

Fig. 13 : Microrotation profiles for various values Up

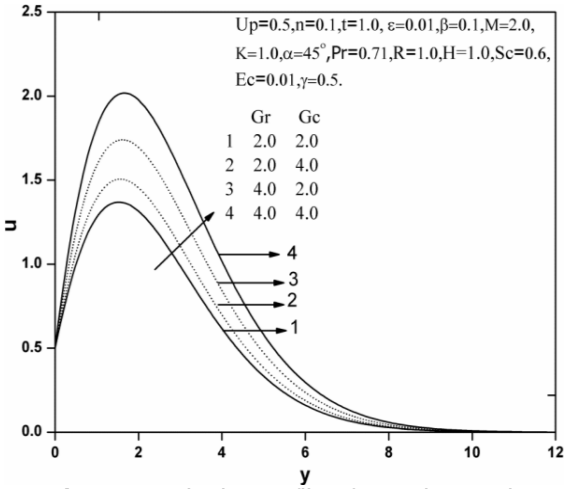

Fig. 14 : Velocity profiles for various values of $Gr \,\&\, Gc$

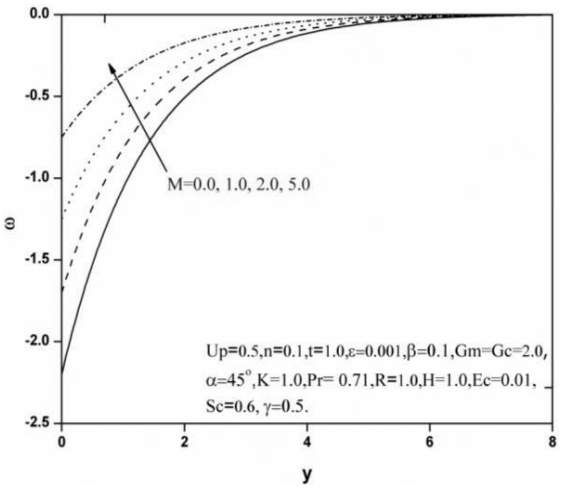

Fig. 17 : Microrotation profiles for various values of M

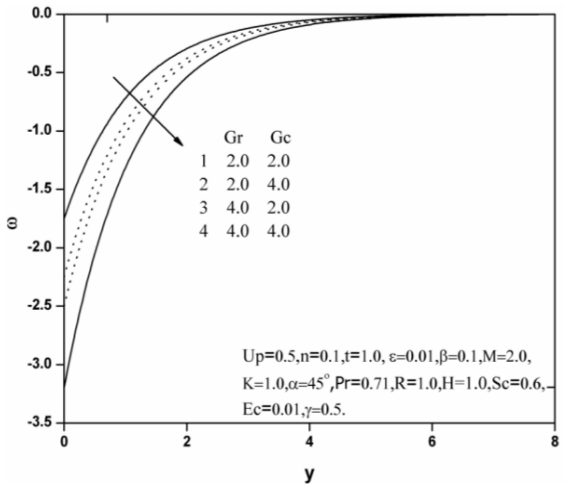

Fig. 15 : Microrotation profiles for various values of $Gr \,\&\, Gc$

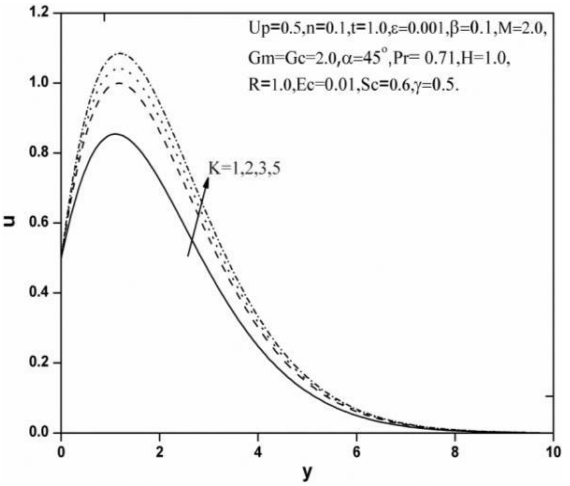

Fig. 18 : Velocity profiles for various values of K

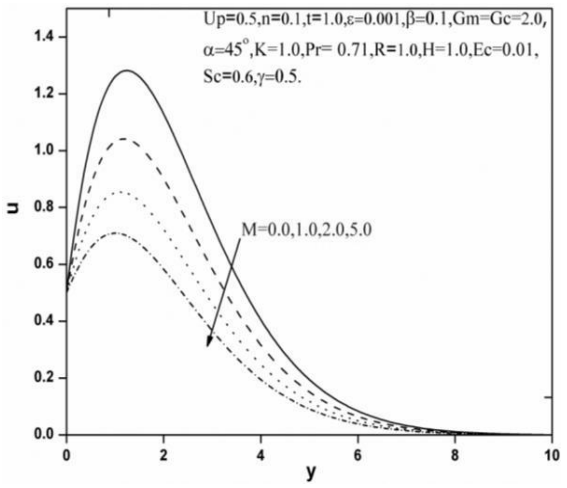

Fig. 16 : Velocity profiles for various values of M

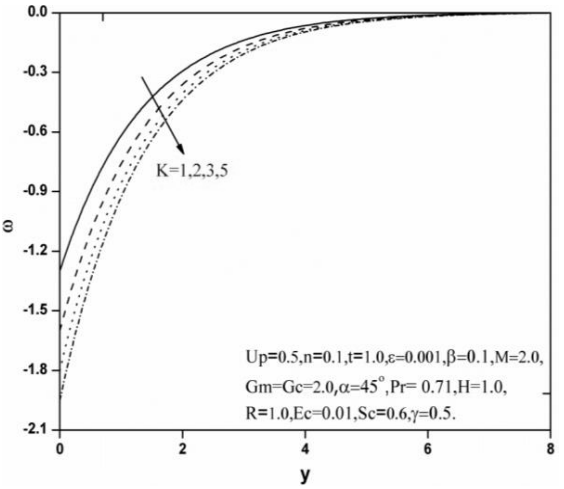

Fig. 19 : Microrotation profiles for various values of K

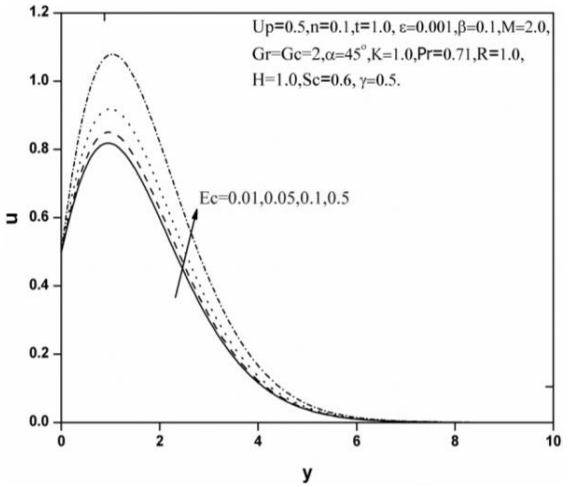

Fig. 20: Velocity profiles for various values of Ec

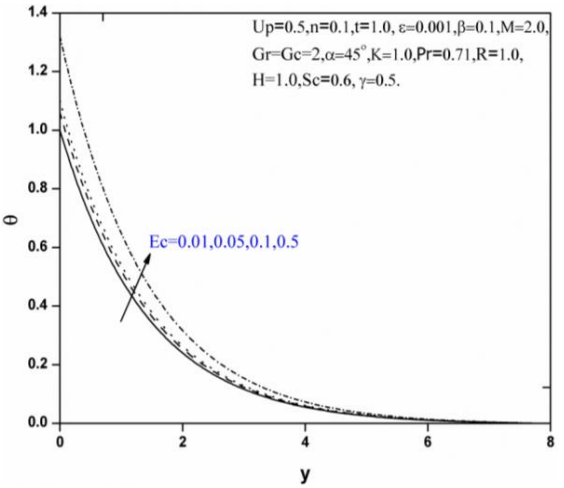

Fig. 21 : Temperature profiles for various values of Ec

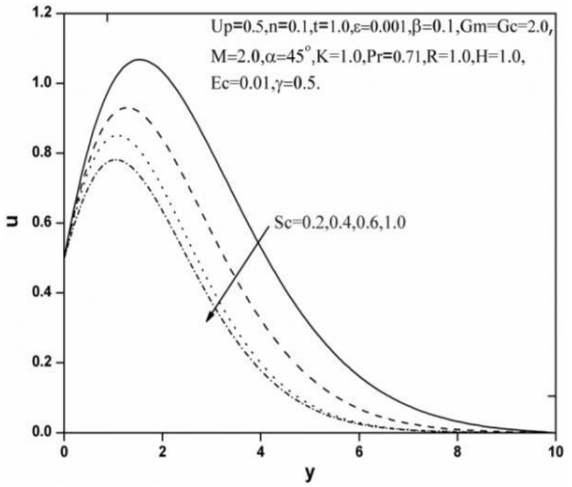

Fig. 22 : Velocity profiles for various values of Sc

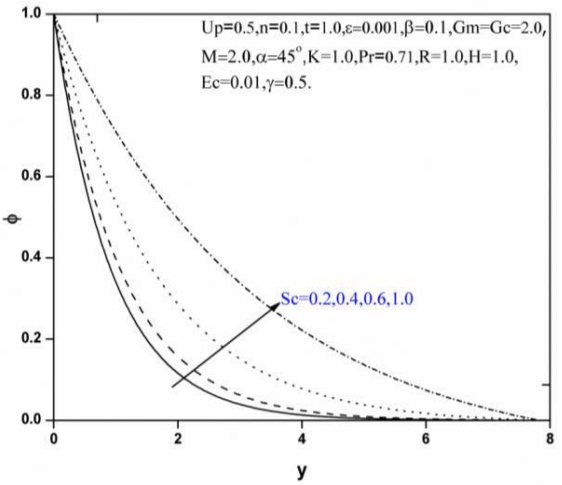

Fig. 23 : Concentration profiles for various values of Sc

5. Conclusions

A mathematical model has been presented for radiative magnetic free convection heat and mass transfer in transient flow of an incompressible, micropolar fluid from an inclined plate in porous media. Heat source/sink and homogeneous chemical reaction effects have been included in the formulation. The conservation equations for momentum, angular momentum (micro-rotation component), energy and concentration have been non-dimensionlized with appropriate variables. The resulting non-linear, transient, coupled system of partial differential equations and set of initial and boundary conditions has been solved numerically, using the variational finite element method with a Galerkin weighted residual scheme. Validation of the finite element solutions for selected cases has been conducted with previous published works i.e. Roja *et al.* [19] and excellent correlation achieved. The computations have been executed in MATLAB software, and have shown that the flow is accelerated and momentum boundary layer thickness decreased with increasing values of U_p, *Gr, Gc, H, K and Ec* but in case of β, α, *M, R, Sc and* γ the flow is decelerated and momentum boundary layer thickness increased. Angular velocity (Microrotation) is suppressed as β, U_p, *Gr, Gc, and K* increases, conversely angular velocity is elevated with α and *M* increases. Increasing heat source/sink *H* parameter and Eckert number *Ec* elevates temperature and enhances thickness of thermal boundary layer. Increasing Schmidt number elevates concentration and enhances the thickness of the species boundary layer. Increasing homogeneous chemical reaction parameter decreases concentration and reduces concentration boundary layer thickness. Sherwood number (wall mass transfer rate) is enhanced with increasing permeability and homogeneous chemical reaction but reduced with increasing angle of inclination of the plate. Wall heat transfer rate is decreased with an increase in heat source/sink (*H*) parameter and increased with an increase in angle of inclination of the plate. With an increase in heat source/sink H parameter there is initially a significant rise in both wall skin friction (flow acceleration) and wall couple stress coefficient (flow acceleration), however with further increase in α,γ there is a subsequent declaration in the flow.

The finite element code developed has resolved efficiently the nonlinear micropolar transport phenomena in inclined plate magnetohydrodynamic heat and mass transfer. Future studies will consider *magnetic induction* effects and will be reported soon.

Acknowledgement

The Authors wish to express their cordial thanks to Reviewers for their valuable suggestions and constructive comments which have served to improve the quality of this paper.

References

[1] A C Eringen *J. Applied Math. Mech* **16** 1 (1996).

[2] A C Eringen *J. Math. Analys. Appl* **38** 480 (1972).

[3] A C Eringen *Micro-continuum field theories II Fluent media,* New York: Springer (2001).

[4] G Lukaszewicz *Micropolar Fluids, Modelling and Simulation,* Boston: Birkhauser Boston (1999).

[5] T Ariman, M A Turk and N D Sylvester *Int. J. Eng. Sci* **11** 905 (1973).

[6] T Ariman, M A Turk and N D Sylvester *Int. J. Eng. Sci.* **12** 273 (1974).

[7] G Swapna, L. Kumar, O. Anwar Bég and Bani Singh *Heat Transfer- Asian Research* **1** (2014). DOI 10.1002/htj.21134.

[8] S Jangili and J.V. Murthy *Front. Heat Mass Transfer* **6(1)** 1 (2015).

[9] S Rawat, R. Bhargava, R. Bhargava and O. Anwar Bég *Proc.IMechE Part C- J. Mechanical Engineering Science* **223** 2341 (2009).

[10] O. Anwar Bég, J. Zueco and T.B. Chang Chemical *Engineering Communications* **198(3)** 312 (2010).

[11] O Anwar Bég, J Zueco, M Norouzi, M Davoodi, A A Joneidi and A F Elsayed *Computers in Biology and Medicine* **44** 44 (2014).

[12] F M Abo-Eldahab and A F Ghonaim *App. Math. Comput.* **169(1)** 500 (2005).

[13] M Ferdows, P Nag, A Postelnicu and K Vajravelu J. App.Fluid. *Mech* **6(2)** 285 (2013).

[14] B I Olajuwon and J I Oahimire *Int. J. Pure and Appl. Math.* **84** 015 (2013).

[15] P K Kundu, K Das and S Jana *Bull. Malays. Math. Sci. Soc* **38** 1185 (2015).

[16] M M Rahman and Y Sultana *Nonlinear Analysis, Modelling and Control* **13** 71 (2008).

[17] P Cheng *Int. J. Heat Mass Transfer* **20** 807 (1977).

[18] P K Singh *Int. J. Scientific. Eng. Research* **3** 2229 (2012).

[19] M. Sudheer Babu, J Girish Kumar and T Shankar reddy *Int. J. Appl. Math. Mech* **9(6)** 48 (2013).

[20] P Roja, T Shankar Reddy and N Bhaskar Reddy *Int. J. Scientific and Research Publications* **3** (2013) Issue **6.**

[21] C H Chen *Acta Mechanica* **172** 219 (2004).

[22] Aurangzaib, A R M Kasim, N F Mohammad and S Shafie Heat *Transfer Asian Research* **42(2)** 89 (2013). DOI: 10.1002/htj.21034.

[23] J Srinivas, J V Ramana Murthy and A J Chamkha *Int.J. Numerical Methods for Heat and Fluid Flow* **26(3)** 1027 (2016). DOI: 10.1108/HFF-09-2015-0354.

[24] S K Bhaumik and R Behera ICCHMT, *Procedia Engineering* **127** 155 (2015). DOI: 10.1016/j.proeng.201.11.318

[25] M K Nayak and G C Dash *Modelling, Measurement and Control B* **84(2)** 1 (2015).

[26] M E M Khedr, A J Chamkha and M Bayomi *Nonlinear Analysis Modelling and Control* **14** 27 (2009).

[27] E Magyari and A J Chamkha *Int. J. Thermal Sci* **49** 1821 (2010).

[28] A J Chamkha and A R A Khaled *Heat and Mass Transfer* **37** 117 (2001).

[29] M M Rahman, M J Uddin and A Aziz *Int. J. Thermal. Sci* **48(3)** 2331 (2009).

[30] D Srinivasacharya and M Upender *Turk. J. Eng. Environmental. Sci* **38** 184 (2015).

[31] S Siva Reddy and MD Shamshuddin ICCHMT, *Procedia Engineering* **127** 885 (2015).

[32] S Siva Reddy and MD Shamshuddin *Theoretical and Applied Mechanics* **43** 117 (2016).

[33] S Rawat, S Kapoor, R Bhargava and O Anwar Bég *Int.J. Computer Applications* **44** 40 (2012).

[34] K Das *Int. J. Numerical Methods in Fluids* **70(1)** 96 (2012).

[35] D Pal and B Talukdar *Central European J. Physics* **10** 1150 (2012).

[36] D Srinivasacharya and M Upender *Chem. Ind. Chem. Eng. Q* **20 (2)** 183 (2014).

[37] T G Cowling, *Magnetohydrodynamics*, New York: Wiley inter Science (1957).

[38] O Anwar Bég *New developments in Hydrodynamics Reaserch, Maximiano J. Ibragimov and A. Anisimov, Eds.,* Ch1. 1, New York: Nova Science (2012).

[39] T Adunson and B Gebhart J. *Fluid Mechanics* **52** 57 (1972).

[40] A Rapits and C Perdikis *ZAMP* **78**, 277 (1998).

[41] R Cortell *Chin Physics Let:* **25** 1340 (2008).

[42] S R Rao *The Finite Element Method in Engineering*, 2nd Edition, BPCC Wheatons Ltd., Exeter USA (1989).

[43] J N Reddy An *Introduction to the Finite Element Method*, New York: McGraw-Hill (1985).

[44] O Anwar Bég, M M Rashidi and R Bhargava *Numerical Simulation in Micropolar Fluid Dynamics* Lambert: 288 pp, Germany: Sarbrucken (2011).

[45] D Gupta, L Kumar, O Anwar Bég and B Singh *Comp.Thermal. Sci.* ***6*** **(2)** 155 (2014).

[46] O Anwar Bég, S Rawat, J Zueco, L Osmond and R S R Gorla *Theoret. Appl. Mech* **41 (1)** 1 (2014).

[47] R Bhargava, S Sharma, P Bhargava, O Anwar Bég and A Kadir *Int. J. Applied Computational Mathematics* (2016). DOI: 10.1007/s40819-106-0180-9 (13 pages).

[48] J Zueco, O. Anwar Bég and H S Takhar *Computational Materials Science* **46(4)** 1028 (2009).

[49] A Mohammadein, M A El-Hakiem, S M M El-Kabeir and M A Mansour *Int. J. Appl. Mechanics Engineering*. **2** 187 (1997).